ORIGINAL RESEARCH ARTICLE

Modeling the buoyancy-driven Black Sea Water outflow into the North Aegean Sea

Nikolaos Kokkos, Georgios Sylaios[*]

Department of Environmental Engineering, Democritus University of Thrace, Xanthi, Greece

Summary   A three-dimensional numerical model was applied to simulate the Black Sea Water (BSW) outflux and spreading over the North Aegean Sea, and its impact on circulation and stratification—mixing dynamics. Model results were validated against satellite-derived sea surface temperature and in-situ temperature and salinity profiles. Further, the model results were post-processed in terms of the potential energy anomaly, ϕ, analyzing the factors contributing to its change. It occurs that BSW contributes significantly on the Thracian Sea water column stratification, but its signal reduces in the rest of the North Aegean Sea. The BSW buoyancy flux contributed to the change of ϕ in the Thracian Sea by 1.23×10^{-3} W m^{-3} in the winter and 7.9×10^{-4} W m^{-3} in the summer, significantly higher than the corresponding solar heat flux contribution (1.41×10^{-5} W m^{-3} and 7.4×10^{-5} W m^{-3}, respectively). Quantification of the ϕ-advective term crossing the north-western BSW branch (to the north of Lemnos Island), depicted a strong non-linear relation to the relative vorticity of Samothraki Anticyclone. Similar analysis for the south-western branch illustrated a relationship between the ϕ-advective term sign and the relative vorticity in the Sporades system. The ϕ-mixing term increases its significance under strong winds (>15 m s^{-1}), tending to destroy surface meso-scale eddies.

* Corresponding author at: Vas. Sofias 12, 67100 Xanthi, Greece. Tel.: +30 25410 79398; fax: +30 25410 79398.
  E-mail address: gsylaios@env.duth.gr (G. Sylaios).

1. Introduction

The North Aegean Sea (NAS) (Fig. 1) acts as a dilution basin, directly affected by the buoyancy outflow of the low-salinity, nutrient-rich Black Sea Water (BSW) exported through the Dardanelles Strait, at the north-eastern part of the basin (Androulidakis and Kourafalou, 2011). Along the Dardanelles, a strongly-stratified two-layer system with opposing flows is formed, consisting of the exiting to the NAS surface BSW layer and the outflowing into the Sea of Marmara bottom layer (Ünlüata et al., 1990). The significant vertical shear stresses developed at the system's interface favor the upward entrainment, thus returning parts of NAS water back to the Aegean (Karnaska and Maderich, 2008). Recent estimates of the annual BSW discharge report values ranging between 38,820 $m^3 s^{-1}$ (Karnaska and Maderich, 2008) and 42,790 $m^3 s^{-1}$ (Tuğrul et al., 2002), with approximately 67% of its volume being directly transferred from the Marmara Sea and 33% attributed to NAS water entrainment. After its outflow, BSW occupies the first 50 m of the water column, overlying on the northward flowing warm and highly saline Levantine Intermediate Water (LIW), between a depth of 50 m and 400 m, and the North Aegean Deep Water (NADW) from 400 m to the bottom (Zervakis et al., 2000). Its impact on surface dynamics of NAS exhibits strong seasonality, especially during early spring, when the mean monthly outflux through the Dardanelles Straits reaches 450 km^3 per season (57,740 $m^3 s^{-1}$), as a result of the increased river runoff and precipitation over the Black Sea and the raised local entrainment fluxes at the Dardanelles (Tuğrul et al., 2002).

The exit of BSW from the Dardanelles produces a cyclonic flow, bifurcating at Lemnos Island, with the southern branch being stronger during the summer, under the influence of the annual northerly Etesian winds, and the northern branch covering the entire Thracian Sea continental shelf (Vlasenko et al., 1996; Zervakis and Georgopoulos, 2002). In winter BSW core concentrates at the northern coast of Lemnos Island, where it bifurcates primarily to the north-west and occasionally to the southwest, under the influence of north-easterly (bora-type) gales. The most prominent surface patterns in NAS include the thermohaline BSW-LIW frontal zone,
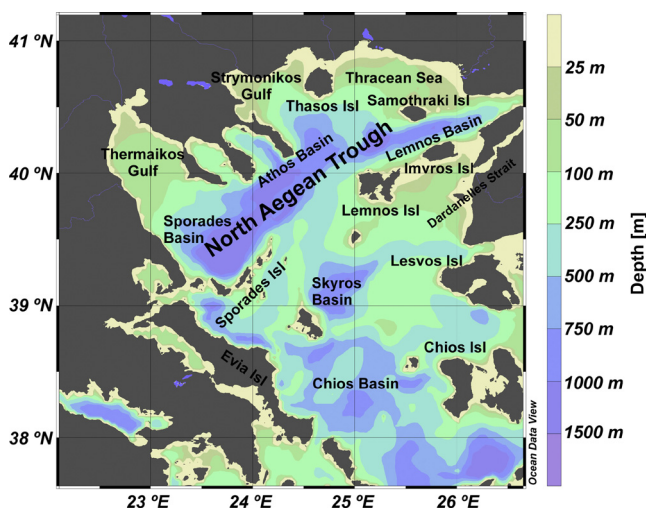
affected strongly by seasonal meteorology (Sylaios, 2011), a semi-permanent anticyclone of variable strength and dimensions developed in the Thracian Sea, around Samothraki and possibly Imvros Islands (Cordero, 1999; Theocharis and Georgopoulos, 1993; Zervakis and Georgopoulos, 2002) and a rapidly changing cyclone—anticyclone system, covering the upper 200 m of the Sporades Basin. This latter system appears supplied either by the higher salinity waters moving from the southern Aegean Sea or by the fresher water of BSW (Kontoyiannis et al., 2003). Other eddy features of variable strength and size appear dependent on BSW discharge and Thermaikos Gulf freshwater outflows (Olson et al., 2007).

Several previous modeling efforts exist, using mostly the Princeton Ocean Model (POM), applied under variable spatial resolution grids and different boundary conditions for the BSW outflux. Zodiatis et al. (1996) used a two-dimensional vertically-integrated model to simulate the synoptic-scale flow patterns of the NAS and utilized NOAA-AVHRR thermal images for model validation. Korres et al. (2002) coupled a high resolution atmospheric model with POM and assessed model's skill in forecasting the satellite-recorded sea surface temperature (SST) field. Kourafalou and Barbopoulos (2003) used the modified sigma-coordinated POM in a high resolution mode (2.5 km × 2.5 km), nested at its southern boundary to a coarse grid Mediterranean model and a regional, intermediate resolution model. BSW discharge boundary condition was determined by the net monthly inflow-outflow budget at the Dardanelles, ranging from 5000 $m^3 s^{-1}$ in December to 15,000 $m^3 s^{-1}$ in June. Kourafalou and Tsiaras (2007) applied POM in a 1.6 km × 1.6 km grid imposing a two-layer (inflow-outflow) transport rate at the Dardanelles boundary. Tzali et al. (2010) applied POM in a series of BSW outflow scenarios, to assess the impact of BSW inflow rate on the established NAS circulation. Finally, Androulidakis and Kourafalou (2011) applied the Hybrid Coordinate Ocean Model (HYCOM) on a very high resolution grid (1/50° × 1/50°) and introduced a new mathematical scheme for BSW outflow rates. Model validation involved the comparison of model results to satellite and in situ data.

The present paper presents the results of a three-dimensional hydrodynamic model for the thermohaline NAS circulation, placing particular emphasis on (a) the model validation procedure, by comparing surface model results with extensive satellite datasets and CTD profiles from field campaigns, (b) the stratification—mixing conditions of BSW along its route over NAS, (c) the quantification of individual terms of the potential energy anomaly general equation, and (d) the description of the permanent and semi-permanent surface meso-scale patterns, developed in NAS and their inter-link to BSW buoyancy spreading.

2. Material and methods

2.1. Model description

The hydrodynamic Estuary and Lake Computer Model (ELCOM), a three-dimensional numerical model developed by the Centre for Water Research at the University of Western Australia (Hodges and Dallimore, 2001) was used for modeling the NAS. This model has mostly been used to simulate the hydrodynamics of lakes and reservoirs, but it has also been

Figure 1 The North Aegean Sea and its physiographic basins.

applied in the modeling of buoyancy fluxes and geophysical flows at large-scale enclosed basins, estuaries and coastal seas, as the Persian Gulf (Alosairi et al., 2011), the Northern Adriatic Sea (Spillman et al., 2007) and the Red Sea (Barry et al., 2009). Kopasakis et al. (2012) modeled successfully NAS water circulation and pollutants accumulation, while Kamidis et al. (2011) validated the model to simulate the transport and diffusion processes in Nestos River plume. Further, Sylaios et al. (2013) utilized the above model-validated results to assess the along- and cross-shore circulation and the stratification-destratification processes in the shallow and elongated Thassos Passage (Thracian Sea).

ELCOM solves the Reynolds-Averaged Navier Stokes equations, using both the hydrostatic and the Boussinesq approximations. The numerical method applies a semi-implicit formulation on a finite-volume framework using rectangular Cartesian cells in an Arakawa-C grid stencil (Hodges, 2000). Horizontal grid spacing is fixed, whereas the vertical spacing may vary as a function of depth, but remains horizontally uniform and fixed over time. Free-surface evolution in each grid cell's column is solved by the vertical integration of the conservation of mass equation for incompressible flow applied to the kinematic boundary condition.

The numerical scheme follows the adapted TRIM approach (Casulli and Cheng, 1992) with modifications for scalar conservation, numerical diffusion, and implementation of a mixed-layer turbulence closure (Hodges, 2000). Convective terms are calculated using a third order Euler–Lagrange scheme, while the ULTIMATE-QUICKEST scheme is introduced for the advection of scalars. The model produces the dynamics of stratified water bodies with external environmental forcing, such as tidal forcing, wind stresses, surface thermal forcing as well as inflows and outflows (Hodges and Dallimore, 2001) and thus seems appropriate for application in NAS. Heat exchange through the water's surface is governed by standard bulk transfer models corrected for non-neutral atmospheric stability effects (Imberger and Patterson, 1990). The model does not follow the commonly-used eddy diffusivity approach, but adopts a unique 1D mixed-layer model for computing the vertical mixing of momentum and scalars (Laval et al., 2003), an approach particularly proper for stratified water bodies as NAS.

2.2. NAS model set-up

2.2.1. Bathymetry and computational domain

Model domain extends from 38.6°N to 41.0°N and from 22.5°E to 27.0°E, thus covering both shelf and deep areas of NAS (Fig. 1). The bottom bathymetry was digitized in a Geographic Information System (MapInfo v10.0), to develop a Digital Elevation Model (DEM) from the Hellenic Navy 1:200,000 bathymetric chart. Model's computational grid was developed using a spatial mapping tool (Vertical Mapper for MapInfo) and the application of linear triangulation interpolation. The modeled area was discretized into a uniform high resolution horizontal grid consisting of 1 km × 1 km orthogonal cells (0.009° × 0.009°), allowing the accurate representation of area's complex bathymetry and topography. The water column at each horizontal cell was divided into 20 exponentially stretched layers, consisting of thinner surface layers with gradually increasing thickness towards

the bottom. All variables were located at fixed z-levels (z-coordinate model), thus producing a computational domain comprised by 3,109,280 rectangular finite-volumes.

2.2.2. Initial and boundary conditions

A constant initial condition over the grid domain ($T = 10$°C and $S = 38.0$ psu) was determined for the ambient water of NAS. Model boundary conditions involved hydrologic, meteorological and tidal forcing. Hydrologic forcing was determined on a mean monthly basis by applying river discharge and water temperature for all main rivers of Greece and Turkey, as reported by Skoulikidis et al. (1998). BSW buoyancy flux was considered seasonally variable, with a mean annual value of 42,222 m^3 s^{-1} or 1331 km^3 yr^{-1}, as computed by Tuğrul et al. (2002). BSW daily temperature was extracted from MODIS SST satellite data for the Sea of Marmara. BSW salinity at the Dardanelles boundary varied seasonally, with a mean annual value of 28.03 psu, following Türkoğlu (2010).

Meteorological time-series for a four-year period (2005–2008) with a 3 hrs time-step were acquired from the NOAA database (http://ready.arl.noaa.gov/READYamet.php) at 1° × 1° spatial resolution, to describe the atmosphere-ocean boundary conditions. Datasets included wind speed and direction, atmospheric relative humidity, cloud cover, barometric pressure, atmospheric temperature, precipitation and solar radiation intensity.

Boundary temperature, salinity, currents and tidal elevations at the southern model boundary were obtained from daily MyOcean products (www.myocean.eu) using the Mediterranean Sea Physics Re-analysis database (1987–2012). Water temperature, salinity and velocity profiles were acquired at 72 layers with a daily time-step at a spatial resolution of 0.0625° along the southern boundary line of the model's computational grid. Initially, these profiles were vertically spline-interpolated to match the layered configuration of ELCOM model. At a second stage, a horizontal interpolation algorithm, applied to each layer, filled the gaps of horizontal model's discretization.

The NAS model was run for four consecutive years with a time-step of 3 min. Year one (2005) was used to develop and stabilize the flow field, especially due to BSW entry, while years 2006–2008 to obtain, compare and post-process model results. These consisted of the three-dimensional flow field, the temperature and salinity fields and the sea-surface height evolution.

2.3. Model validation procedure and criteria

Model validation was achieved in two manners: (a) by comparing sea-surface temperature model results at 44 regularly-spaced model grid cells with the SST data obtained by the International Group for High Resolution SST (GHRSST, www.ghrsst.org), a platform combining daily updates of near-real-time level 2 data (SSTs at observed pixels), level 3 data (gridded in space, but with no gap-filling) and level 4 data (gap-free objective analysis data), with a 0.25° × 0.25° spatial resolution (Martin et al., 2012); and (b) by comparing model produced temperature and salinity profiles with the 2006 CTD casts of summer NAS cruises (Sylaios, 2011; Sylaios, unpublished data).

To evaluate the validity of model results with satellite and in-situ data, a set of criteria was established (Jedrasik, 2005):

(a) the correlation coefficient, r, defined as:

$$r = \frac{\text{cov}(o_i, m_i)}{\sigma_o \sigma_m} = \frac{\overline{o_i m_i} - \overline{o}\,\overline{m}}{\sigma_o \sigma_m}, \tag{1}$$

where o_i and m_i represent the observed and modeled paired values (with $i = 1, 2, \ldots, N$), respectively, and $\overline{o}$, $\overline{m}$ and σ_o and σ_m the respective means and standard deviations of the observed and modeled datasets. This is the non-dimensional measure of co-variation of the observed and modeled values, reaching its maximum at unity. Such criterion is insensitive to the total model bias.

(b) the mean squared error, MSE, defined as:

$$\text{MSE} = \sigma_o^2 \left[(1 - r^2) + \left(\frac{\sigma_m}{\sigma_o} - r \right)^2 + \frac{(\overline{m} - \overline{o})^2}{\sigma_o^2} \right], \tag{2}$$

where the first term is the squared correlation coefficient; the second term describes the conditional model bias C, expressing the correlation between model error and the values simulated by the model; and the third term the unconditional model bias B, defined as the ratio of absolute bias to the squared standard deviation of the observations. For increased model reliability MSE should be minimum.

(c) the Nash-Sutcliffe effectiveness coefficient E, defined as:

$$E = 1 - \frac{\text{MSE}}{\sigma_o^2}. \tag{3}$$

It is considered as a dimensionless transformation of MSE, also called a quadratic model score. Its value increases up to unity with increasing model quality.

(d) the special correlation coefficient:

$$R_s = \sqrt{1 - \frac{\text{MSE}}{\sigma_o^2 + \overline{m}^2}}. \tag{4}$$

A perfect fit is reached when $R_s = 1$, meaning that MSE = 0. R_s better represents the fitting of model simulations to the observed ones, compared to the total square error (Jedrasik, 2005), and

(e) the mean modified model bias, defined as the ratio of the mean modeled to the mean observed counterpart, indicating the over- or under-estimation tendency of the simulations.

2.4. Model results post-processing

To assess the impact of BSW buoyancy flow path over the near-surface water column (0−200 m depth) of NAS, the potential energy anomaly ϕ (PEA, in J m^{-3}) was considered through model results. PEA-values express the stability of the water column, defined as the amount of energy per unit volume needed to vertically homogenize the water column, as (Simpson, 1981):

$$\phi = \frac{1}{h} \int_{-h}^{0} gz(\overline{\rho} - \rho)\, dz, \tag{5}$$

where g is the gravitational acceleration [m s^{-2}], z is the vertical coordinate pointing upward at the sea surface [m], $\overline{\rho}$ is the depth-averaged density [kg m^{-3}], ρ is the local density [kg m^{-3}] at depth z, and h is the total water depth [m]. By definition ϕ is depth independent, but it varies horizontally and in time. It occurs that ϕ is zero for a fully-mixed water column, and positive for stable stratification.

Although PEA explains the instant state of water column in terms of mixing and stratification, the temporal change of PEA may explain the interacted processes related to mechanical mixing (wind and tidal stirring) and stratifying mechanisms as the solar heat flux and the freshwater buoyancy flux (Simpson et al., 1991). Therefore, the change of PEA in time may be expressed as:

$$\left\{ \frac{\partial \phi}{\partial t} \right\}_{\text{TOTAL}} = -\frac{\delta k_s \rho_a |W^3|}{h} - \frac{\epsilon k_b \rho_w |u_b^3|}{h} + \frac{\alpha g Q_S}{2 C_p} + \frac{1}{320}$$
$$\times \frac{g^2 h^4}{N_Z \rho_w} \left(\frac{\partial \rho_w}{\partial x} \right)^2, \tag{6}$$

where the first term represents the wind stirring influence and the second term represents the tidal stirring effect, both tending to decrease ϕ over time. δ and ε are empirically determined mixing coefficients ($\delta = 0.039$ and $\varepsilon = 0.0038$) expressing the efficiency in the conversion of wind and the tidally-generated turbulent kinetic energy into potential energy (Lund-Hansen et al., 1996), k_s and k_b are the surface and bottom drag coefficients ($k_s = 6.4 \times 10^{-5}$ and $k_b = 2.5 \times 10^{-3}$), ρ_a is the air density (1.2 kg m^{-3}), ρ_w is the water density [kg m^{-3}], h is the water column depth [m] and W and u_b represent the wind speed [m s^{-1}] and bottom current velocity [m s^{-1}]. The third and fourth terms express the stratifying solar heat flux and freshwater buoyancy flux, respectively, tending to increase the ϕ-value in time. α and C_p are thermal expansion coefficients ($\alpha = 1.6 \times 10^{-4}$°C^{-1} at 9°C and $C_p = 4.0 \times 10^3$ J kg^{-1} °C^{-1}), g is the gravity acceleration [m s^{-2}], Q_S is the incident solar heat flux at the sea surface [W m^{-2}] and N_Z is the vertical eddy viscosity coefficient [m^2 s^{-1}], determined as $N_Z = \gamma h u$, where $\gamma = 3.3 \times 10^{-3}$ and u the depth-averaged tidal speed [m s^{-1}].

In order to derive the relative impact of each individual term on the change of the potential energy anomaly of NAS water column, the combined Eq. (6) was integrated in time, for a period of a month, using the mean daily values of respective parameters, thus:

$$\phi_{\text{TOTAL}} = -\delta k_s \rho_a \left(\frac{1}{h} \right) \int_0^t |W|^3\, dt + \frac{\alpha g}{2 C_p} \int_0^t Q_S\, dt + \frac{1}{320}$$
$$\times \frac{g^2 h^4}{N_Z \rho_w} \int_0^t \left(\frac{\partial \rho_w}{\partial x} \right)^2 dt - \epsilon k_b \rho_w \frac{1}{h} \int_0^t |u_b|^3\, dt, \tag{7}$$

where terms 1 to 4 refer to the relative impact of the wind, the incident solar radiation, the BSW buoyancy flux and the tide on the total potential energy anomaly of the water column. The term $(\partial \rho_w / \partial x)$ refers to the model-computed depth-averaged (0−200 m) density gradient between BSW exit point at the Dardanelles and each selected studied site throughout NAS. The impact of the tidal term was considered as negligible for the micro-tidal environment of NAS.

2.5. Relative contribution of PEA equation terms along a meridional transect

To comprehend the impact of advection of BSW pulses on NAS, the relative magnitude of each term in the general dynamic ϕ-equation was quantified, utilizing the ELCOM model results for the upper 130 m layer, corresponding to the upper 5 layers, along a meridional transect. The general ϕ-equation derived by Burchard and Hofmeister (2008) reads:

$$\frac{\partial \phi}{\partial t} = \underbrace{-\nabla_h(\overline{\boldsymbol{u}}\phi)}_{A} + \underbrace{\frac{g}{h}\nabla_h\overline{\rho}.\int_{-h}^{0}\tilde{u}z\,dz}_{B} - \underbrace{\frac{g}{h}\int_{-h}^{0}\left(\eta - \frac{h}{2} - z\right)\tilde{\boldsymbol{u}}\cdot\nabla_h\tilde{\rho}\,dz}_{C}$$

$$-\underbrace{\frac{g}{h}\int_{-h}^{0}\left(\eta - \frac{h}{2} - z\right)\tilde{w}\partial_z\tilde{\rho}\,dz}_{D} + \underbrace{\frac{\rho_0}{h}\int_{-h}^{0}P_b\,dz}_{E} - \underbrace{\frac{\rho_0}{2}(P_b^s + P_b^b)}_{F}$$

$$+\underbrace{\frac{g}{h}\int_{-h}^{0}\left(\eta - \frac{h}{2} - z\right)Q\,dz}_{G} + \underbrace{\frac{g}{h}\int_{-h}^{0}\left(\eta - \frac{h}{2} - z\right)\nabla_h(K_h\nabla_h\rho)\,dz}_{H},$$

(8)

where $\overline{u}$ and $\tilde{u}$ are the depth-averaged and the deviation from the depth-mean horizontal velocity vectors, respectively [m s^{-1}], $\tilde{w}$ is the deviation from depth-mean vertical velocity [m s^{-1}], η is the elevation of sea surface above the mean [m], $\overline{\rho}$ and $\tilde{\rho}$ are the depth-averaged and the deviation from the depth-mean densities, respectively [kg m^{-3}], ρ_0 is the reference density [kg m^{-3}], Q is the source term for density due to heating [W m^{-2}], K_h is the horizontal eddy diffusivity [m^2 s^{-1}], P_b is the vertical buoyancy flux ($=(g/\rho_0)K_z(\partial\rho/\partial z)$), while P_b^s and P_b^b are the surface and bottom buoyancy fluxes [m^2 s^{-3}], respectively, and ∇_h is the horizontal gradient operator.

In the above equation the described processes are: ϕ-advection (term A), representing the advection of potential energy anomaly by the depth-averaged horizontal velocity vector; the depth-mean straining (term B), representing the straining of the depth-averaged horizontal density gradient due to the deviation from the depth-mean velocity vector; the non-mean straining (term C), representing the straining produced by the deviation from the depth-averaged horizontal density gradient; the vertical advection (term D), produced by the deviation from the linear vertical velocity proceeding from the kinematic boundary conditions imposed on the water column surface and bottom; the vertical mixing (term E), expressed by the integrated vertical buoyancy flux; the surface and bottom density fluxes (term F), both increasing ϕ; the heating due to short-wave radiation (term G), representing inner sources or sinks of potential density; and the divergence of horizontal turbulent density fluxes (term H), increasing ϕ at the upper half of the water column.

For our analysis, only terms A, B, C, E, F and G were accounted for as the most important factors controlling the stratification—mixing dynamics of the area. Following Hoitink et al. (2011), contributions from the temporal and spatial variations of vertical velocity in the deviation of mean density (term D) and the impact on stratification from the horizontal divergence of horizontal turbulent density fluxes (term H) were considered as negligible.

Term E (vertical mixing) was simplified into:

$$\left(\frac{\partial\phi}{\partial t}\right)_{\text{Term-E}} = -C_d\Gamma\rho_0\frac{|\overline{u}^3|}{h},$$

(9)

where C_d is the drag coefficient (=0.0025) and Γ is the mixing efficiency coefficient (=0.04).

Terms F and G involving inner sources of density due to absorption of solar radiation and the surface and bottom buoyancy fluxes appear dominated by surface heating. These terms could be parameterized according to Wiles et al. (2006), involving meteorological data (derived from NOAA database) as the incoming short wave radiation, relative humidity, wind speed and sea albedo for the derivation of the upward heat flux due to evaporation, the long-wave back radiation and the sensible heat transfer, as following:

$$\left(\frac{\partial\phi}{\partial t}\right)_{\text{Terms F\&G}} = \frac{\alpha g}{2C_p}(Q_S'T - Q_u),$$

(10)

where C_p is the heat capacity (=4.0×10^3 J kg$^{-1\circ}$C^{-1}), α is the thermal expansion coefficient (=1.51×10^{-4} K^{-1}), Q_S' is the sub-surface incident solar radiation, T is the heat released when radiation reaches the sea bottom, and Q_u is the sum of upward heat flux due to evaporation, long-wave back-radiation and sensible heat flux ($Q_u = Q_E + Q_B + Q_C$). Q_S' is determined by $Q_S' = Q_S(1-A)$, where A is the sea surface albedo (=0.15) and Q_S is the incident solar radiation. T is computed as a function of the effective diffusive attenuation coefficient for short wave radiation ($k = 0.3$) and total water depth, as:

$$T = 1 - \frac{2(1-\alpha_1)}{kh}(1-e^{-kh}),$$

(11)

where $\alpha_1 = 0.55$, representing the fraction of heat absorbed at the thin surface layer. The upward heat flux terms were determined using relative humidity and wind velocity data from NOAA database combined with sea surface temperature data from the ELCOM model and applying the standard heat flux formulas (Gill, 1982). All calculations were performed in MATLAB 10.

3. Results

3.1. Model results validation

At the first validation stage, daily-averaged SST model results were compared to satellite recorded SST daily data obtained from the GHRSST dataset ($n = 365$ per year). For each station, the produced scatter points followed closely the diagonal in the simulated—observed data plots (Fig. 2a and b), providing quite successful statistical measures. The spatially-mean validation criteria, presented in Table 1, indicate that model's performance improves over time (years 2006—2008). Mean conditional and unconditional model biases of the mean squared error for all these years were computed at 0.040 and 0.099, respectively. From years 2006 to 2008 the mean modified model bias turns from over- to slight under-estimation of the satellite-derived SST (Table 1). This performance varies spatially and temporally. In the Thracian Sea slight winter and autumn over-estimation exists, changing to fair under-estimation in spring and summer (Fig. 2c). Summer under-estimation appears more prominent in the Sporades
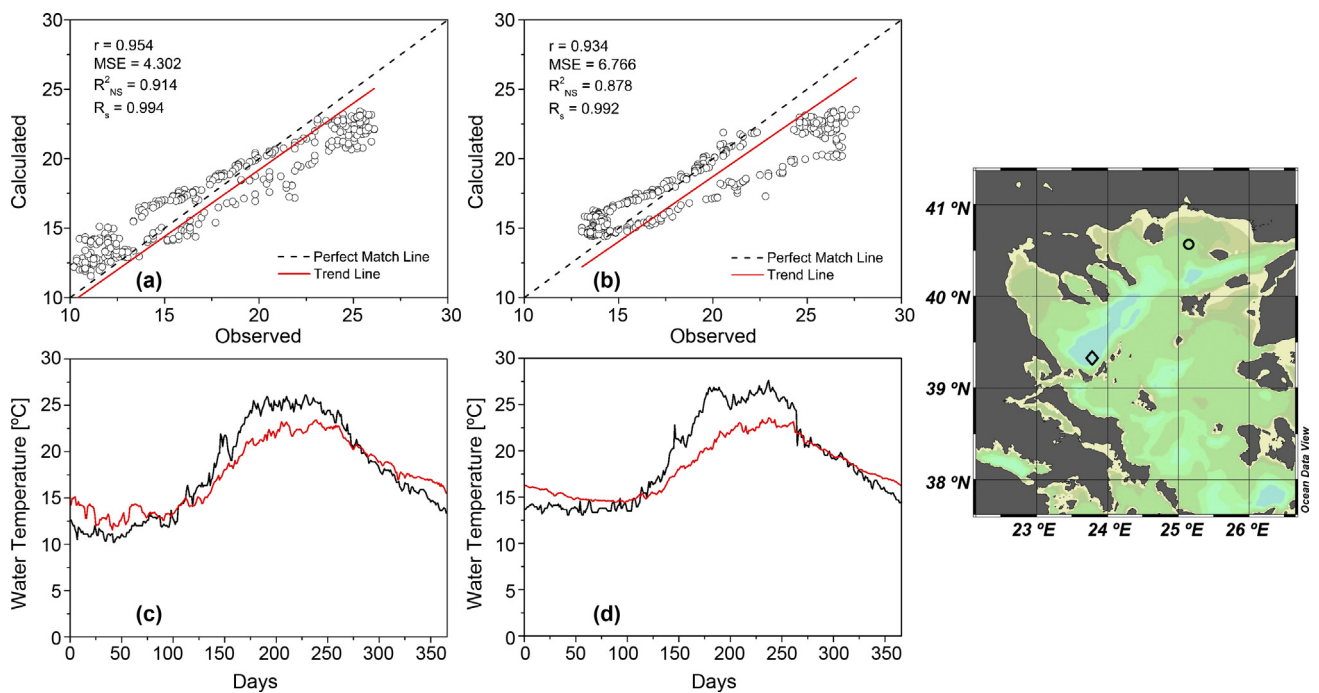
Figure 2 Scatter diagrams and temporal variability between the modeled and the GHRSST sea-surface temperature data during 2008. Subplots (a) and (c) compare data in the Thracian Sea (circle), and (b) and (d) in the Sporades Basin (diamond).

Basin (Fig. 2d). Such underestimation could also be attributed to the daily-averaging of modeled data, the impact of relatively poor meteorological conditions resolution and the fixed horizontal eddy viscosity and diffusivity coefficients. Fig. 3 illustrates the spatial variability in the model validation statistical measures for year 2008. Higher correlation coefficients were obtained in the Thracian Sea and Thermaikos Gulf, where the model slightly under-estimated observations. Lower correlation but improved modified bias was achieved in the central parts of NAS and in the Chios Basin.

Table 1 Spatially-mean statistical measures for ELCOM model validation in terms of SST.

Parameter	2006	2007	2008
Satellite-derived SST			
Correlation coefficient, r	0.917	0.924	0.941
Mean squared-error, MSE	4.985	5.060	3.838
Nash-Sutcliffe effectiveness coefficient, E	0.774	0.779	0.818
Special correlation coefficient, R_s	0.993	0.993	0.995
Modified model bias, MMB	1.063	1.024	0.966

	Temperature	Salinity
Year 2006 CTD casts		
Correlation coefficient, r	0.859	0.794
Mean squared-error, MSE	6.410	1.383
Nash-Sutcliffe effectiveness coefficient, E	0.402	0.138
Special correlation coefficient, R_s	0.990	0.999
Modified model bias, MMB	0.921	0.975

At the second validation stage, the model's ability to reproduce the vertical distribution of temperature and salinity fields was tested. Year 2006 CTD casts in NAS (103 sampling sites) were compared to temperature and salinity model results, up to 200 m depth. In-situ data were initially layer-averaged, to match model discretization, and then directly compared to model outputs ($n = 457$). Validation statistics shown in Table 1 indicate a rather good agreement and a fair under-estimation of in-situ observed variables. Indicative comparative profiles of water temperature and salinity for sites in Thracian Sea and Sporades Basin are shown in Fig. 4.

3.2. Model results description

The simulated surface flow exhibits similar patterns to those produced by other recent NAS models (Androulidakis and Kourafalou, 2011; Androulidakis et al., 2012; Kopasakis et al., 2012) and in-situ observations (Eronat and Sayin, 2014; Sayin et al., 2011; Sylaios, 2011). In winter (09 February 2008), the Dardanelles low salinity flow bifurcates around Lemnos Island, with its northern branch crossing the Lemnos-Imvros Passage, moving eastwards towards Chalkidiki Peninsula (Fig. 5). The flow around Athos Peninsula and into Singitikos Bay agrees to the Lagrangian observations of Olson et al. (2007). Under Ekman transport, the southern Dardanelles branch flows around the southern coasts of Lemnos Island, turning westwards to feed a weak anticyclone in the Sporades Basin. This pattern is consistent to the observations made by Olson et al. (2007) using drifters when reported on the enhanced westward Ekman drift associated with the strong northerly winds. A strong anti-cyclonic flow with a large diameter (∼70 km) is formed in the vicinity of the BSW-LIW front, to the north-west of Lesvos Island.
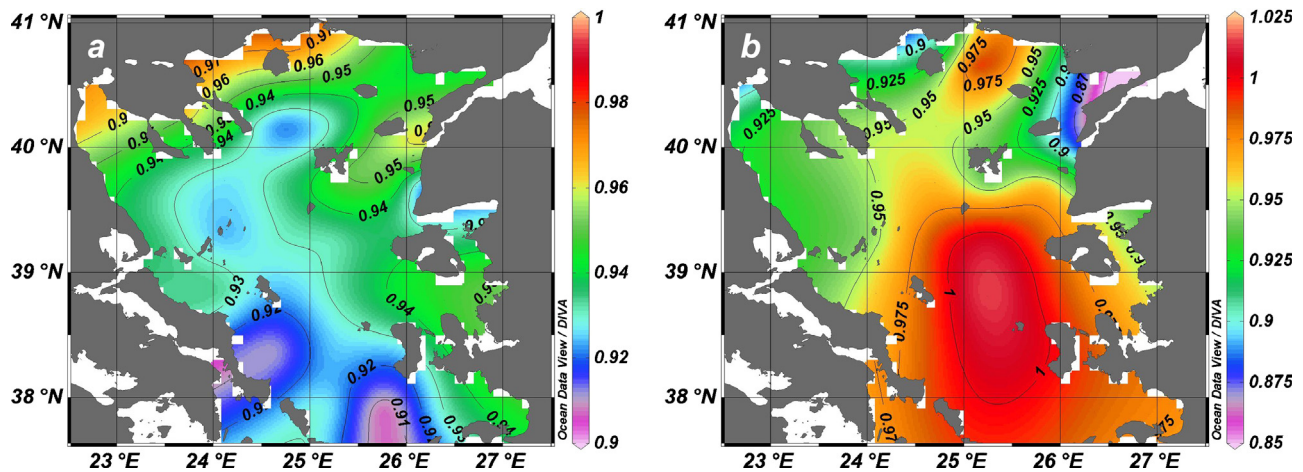
Figure 3 Spatial variability of (a) the correlation coefficient and (b) the modified model bias, between the modeled and the GHRSST sea-surface temperature datasets.

In spring (08 May 2008) the wind influence lessens and as BSW outflow remains at substantial levels ($\sim$50,000 m^3 s^{-1}), its northwestern branch achieves speeds up to 1 m s^{-1}, strongly affecting the Thracian Sea (Fig. 6). This low salinity water ($\sim$33.7–34.5) forms the Samothraki Anticyclone, a distinctive feature in Thracian Sea. Part of the BSW flow reaches the southwestern part of Thassos Island, and bifurcates into a branch moving towards Strymonikos Gulf and another towards Athos Peninsula. Similar features were also produced by the model of Androulidakis et al. (2012).

A circulation snapshot representing the summer conditions of moderate south-eastern winds and diminished BSW outflow is shown in Fig. 7 (05 July 2008). BSW flow follows a westward pathway between Lemnos and Imvros Islands, with speeds ranging from 0.7 to 0.95 m s^{-1}. As flow moves northwards

towards Thassos Island, it separates developing a twin cyclonic–anti-cyclonic system to the west and north-west of Samothraki Island. This twin cyclone–anticyclone system was also simulated by Androulidakis et al. (2012) during the summer period (August 2003). The BSW-LIW frontal zone was found to the south and east of Lemnos Island, allowing the southwestern water transfer towards Skiros Basin. Again, Androulidakis et al. (2012) points out the strong south-western propagation of surface waters and the presence of Sporades Anticyclone during the entire summer.

## 3.3. PEA distribution and change

The PEA quantifies the deficit in the potential energy due to stratification over a water column of 200 m depth, as
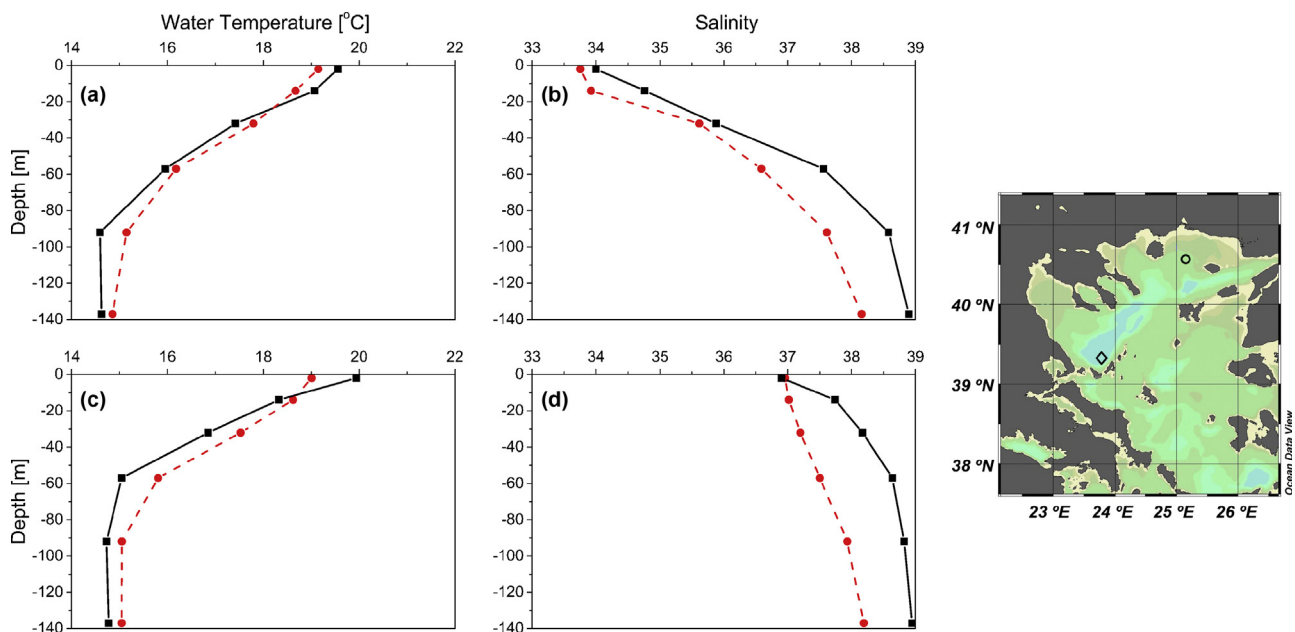
Figure 4 Modeled and observed profiles (surface to 200 m depth) in the Thracian Sea (circle) for (a) water temperature and (b) salinity and in the Sporades Basin (diamond) for (c) water temperature and (d) salinity, in summer 2006.
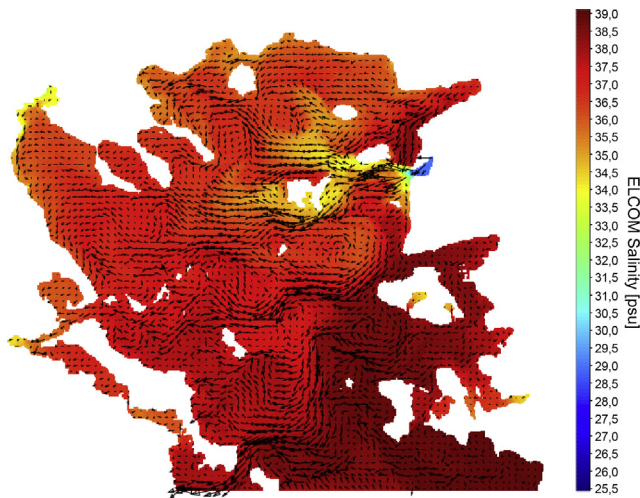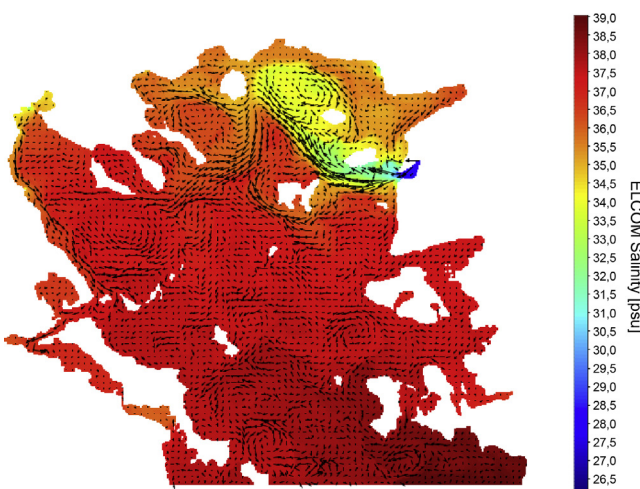
Figure 5 Surface flow and salinity patterns in the North Aegean Sea as produced by ELCOM model on 09 February 2008.
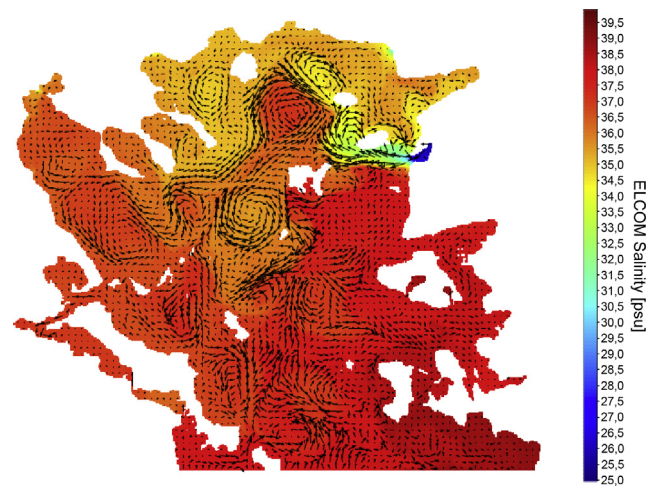
Figure 7 Surface flow and salinity patterns in the North Aegean Sea as produced by ELCOM model on 05 July 2008.

compared to that of the fully mixed water column. The PEA distribution in NAS increases due to the BSW buoyancy outflux and the solar radiation effect and diminishes under the wind mixing influence. Fig. 8 presents the PEA temporal variability at selected sites in the Thracian Sea, in Lemnos Basin, to the south of Lemnos Island and in Sporades Basin for year 2008. Results illustrate the PEA characteristic bell-shaped curve resulting from the incident heat flux seasonality. In the Thracian Sea and Lemnos Basin sites, the sudden PEA changes are attributed to increased BSW bulges reaching the site (positive change) and to wind impact and the LIW originated masses entrapped through eddies at the site (negative change). For example, the significant PEA reduction produced in the Thracian Sea and Lemnos Basin between 26 June 2008 and 04 July 2008 is attributed to the intrusion and entrapment of saltier Levantine origin water, while wind mixing ($\sim$10 m s^{-1}) is responsible for a similar sudden change on 12 October 2008. Moving to the south of Lemnos Island and towards Sporades Basin, the impact of BSW on the water
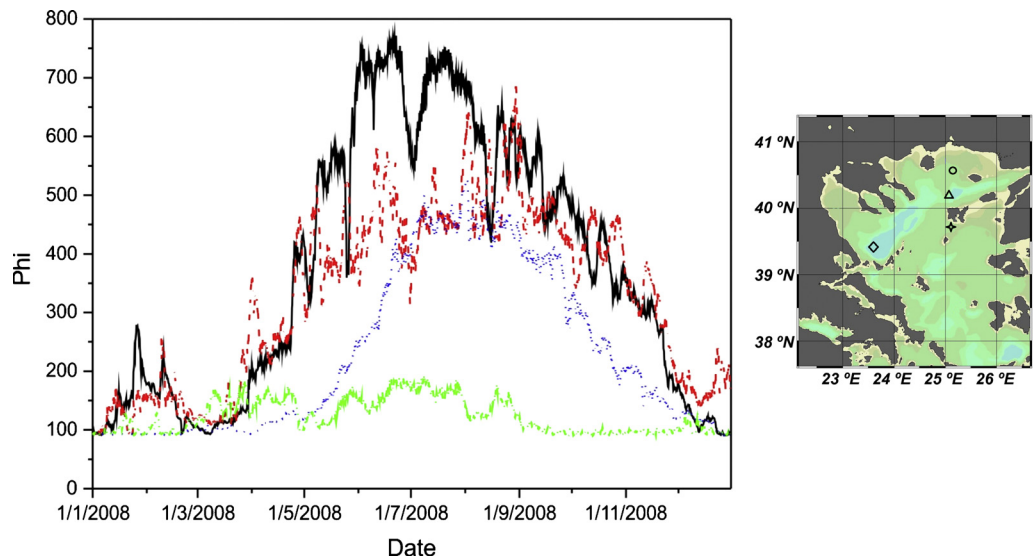
column stratification reduces, and PEA values peak at 650 J m^{-3} and 580 J m^{-3}, respectively.

To understand the mechanisms responsible for the stratification—mixing dynamics over NAS, the individual terms of Eq. (6) were explored and their relative contribution on ϕ-change was accounted for. In the Thracian Sea, during January 2008, mean water column density of 1028.11 kg m^{-3}, mean density gradient of 1.41×10^{-5} kg m^{-4}, mean wind speed of 5.8 m s^{-1} and mean solar radiation of 92 W m^{-2} were considered. The wind impact on ϕ-change may be estimated at 3.62×10^{-6} W m^{-3}, the influence of solar radiation is an order of magnitude higher (1.41×10^{-5} W m^{-3}), while the buoyancy flux effect induced by BSW contributes the most (1.23×10^{-3} W m^{-3}). During July 2008, solar heat flux reached 330 W m^{-2} thus depth-averaged density reduced to 1026.80 kg m^{-3}, while the depth-averaged density gradient decreased slightly at 1.18×10^{-3} kg m^{-4}. As wind speeds decreased, the wind effect on ϕ-change reached 2.1×10^{-6} W m^{-3}, the influence of solar heat flux increased approximately by a factor of four (7.4×10^{-5} W m^{-3}), while the BSW impact almost halved compared to winter (7.9×10^{-4} W m^{-3}), but remained the dominant stratification mechanism.

Integrating the above results over a monthly period during 2006—2008, the relative contribution of each term on the total PEA may be examined. Table 2 presents the mean monthly ϕ-values for Thracian Sea, as obtained from calculated vertical density distribution and the use of Eq. (5), and the integrated monthly ϕ-values as obtained through Eq. (7). The results obtained by both methods appear rather comparative. Moreover, the relative contribution of each mechanism (solar radiation, buoyancy effect and wind impact) on the mean-monthly PEA value is also shown. The solar radiation contribution on the water column PEA depicts an average value of 130.79 J m^{-3}, ranging between 55.28 J m^{-3} in January and 55.86 J m^{-3} in December up to 208.02 J m^{-3} in July. These findings appear in agreement with the North Aegean sea-atmosphere heat fluxes analysis developed by Poulos et al. (1997) and Androulidakis et al. (2012). In the same month, the BSW buoyancy contribution

Figure 6 Surface flow and salinity patterns in the North Aegean Sea as produced by ELCOM model on 08 May 2008.

Figure 8 Temporal change of the potential energy anomaly at (a) the Thracian Sea (solid black line), (b) the Lemnos Basin (red dashed line), (c) the south of Lemnos Island (blue dotted line) and (d) the Sporades Basin (green dashed-dotted line) during 2008. The map shows the exact location of stations at the Thracian Sea (circle), the Lemnos Basin (triangle), the south of Lemnos Island (star) and the Sporades Basin (diamond). (For interpretation of the references to color in this figure legend, the reader is referred to the web version of this article.)

also receives its maximum value (611.98 J m^{-3}), leading to the most stratified water column having a ϕ-stratification value of 811.27 J m^{-3}. The wind impact reaches its maximum ϕ-contribution in January (22.19 J m^{-3}), producing a rather well-mixed water column in the Thracian Sea, since the ϕ_{TOTAL} value is limited to 94.94 J m^{-3}.

3.4. Quantification of PEA equation terms

Fig. 9 presents the temporal variation in the magnitude of the examined potential energy equation terms crossing the Northern Lemnos—the Thracian Sea meridional transect during 2008 (A: 40.475°N, 25.241°E; B: 40.022°N, 25.241°E). The $d\phi/dt$ term varies between -1.014×10^{-4} W m^{-3} and $+1.389 \times 10^{-4}$ W m^{-3} (Fig. 9a), while the ϕ-advective term,

accounting for the effect of BSW buoyancy outflux crossing the transect in the east-to-west direction (positive values), ranges from -0.914×10^{-4} W m^{-3} to $+3.926 \times 10^{-4}$ W m^{-3}. Positive values prevail throughout the year, indicating that BSW is mostly transferred westward, towards the Thracian Sea (Fig. 9b). This westward transferred ϕ-advective flux appears related to the presence of Samothraki Anticyclone, an eddy system with 50—60 km diameter spread over the Thracian Sea. The depth-mean straining term, explained as the effect of tidal shear on the vertically constant horizontal density gradients appears of lower magnitude than the ϕ-advective term, ranging between -0.671×10^{-5} W m^{-3} and $+0.440 \times 10^{-5}$ W m^{-3} (Fig. 9c). Similarly, limited is the variability of the non-mean straining (term C), while the vertical mixing term (term E, Fig. 9e), expressed as

Table 2 The Thracian Sea mean monthly PEA, as computed by model results and monthly-integrated PEA and relative PEA-contribution of individual terms as derived from Eq. (7) during 2006—2008.

| Months	Mean monthly PEA [J m^{-3}]	ϕ_{TOTAL} [J m^{-3}]	ϕ_{SOLAR} [J m^{-3}]	$\phi_{BOUYANCY}$ [J m^{-3}]	ϕ_{WIND} [J m^{-3}]
January	103.83	94.94	55.28	62.27	22.19
February	104.04	115.97	70.55	54.89	9.17
March	224.71	206.22	120.10	95.87	9.57
April	308.49	317.18	156.73	163.05	2.57
May	613.32	601.80	206.76	398.15	3.08
June	786.51	673.00	200.03	475.02	2.02
July	755.01	811.27	208.02	611.98	8.70
August	774.92	761.55	195.60	567.40	1.42
September	662.56	633.02	141.20	497.36	5.51
October	431.28	455.27	96.64	368.29	9.64
November	249.55	292.79	62.79	235.60	5.56
December	163.08	172.46	55.86	121.66	5.03
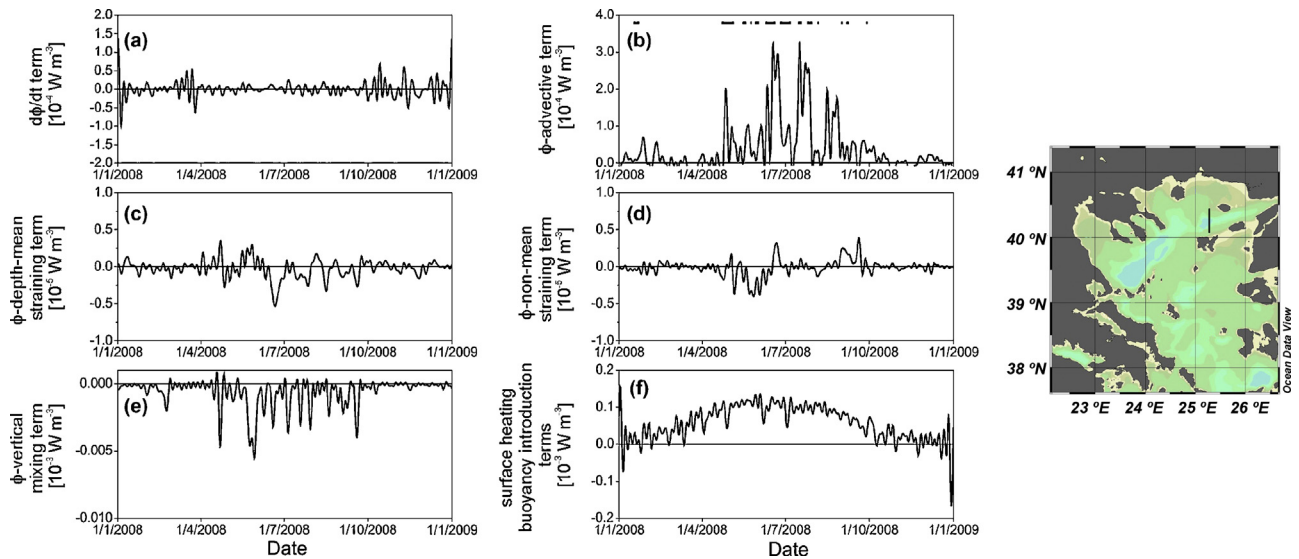
Figure 9 Temporal variability of (a) the $d\phi/dt$-term ($\times 10^{-4}$ W m^{-3}), (b) the ϕ-advective term ($\times 10^{-4}$ W m^{-3}), (c) the ϕ-depth-mean straining term ($\times 10^{-5}$ W m^{-3}), (d) the ϕ-non-mean straining term ($\times 10^{-5}$ W m^{-3}), (e) the ϕ-vertical mixing term ($\times 10^{-3}$ W m^{-3}) and (f) the surface heating buoyancy introduction terms ($\times 10^{-3}$ W m^{-3}), crossing the north-west BSW branch. All terms were smoothed using a low-pass-filter of 0.2 Hz cutoff frequency. Black lines in subplot (b) represent periods of Samothraki Anticyclone presence in Thracian Sea.

the integrated vertical buoyancy flux, fluctuates between near zero and -0.012×10^{-3} W m^{-3}, obtaining increased negative values under the influence of strong southern and north-eastern winds (15—20 m s^{-1}). The impact of solar heating, dominating terms G & F, increases during the summer obtaining a maximum value of 0.155×10^{-4} W m^{-3} and reduces to near zero values in the winter (Fig. 9f).

The variability of the ϕ-equation terms crossing an indicative meridional transect for the BSW south-western branch (C: 39.573°N, 25.241°E; D: 39.123°N, 25.241°E), is shown in Fig. 10. The positive sign in the ϕ-advective term (Fig. 10b)

is related to the strengthening of the SW branch, with increased flow up to 0.6 m s^{-1} moving from the south-eastern cape of Lemnos towards Agios Efstratios Island. The Sporades anticyclone appears mostly supported by high positive ϕ-advective values, as on 09 March 2008 when $U_{\text{SW-branch}} = 0.72$ m s^{-1}, the $\phi_{\text{advective}}$ term $\sim 0.60 \times 10^{-4}$ W m^{-3} and an anticyclonic flow is formed in Sporades (Fig. 11a). Similar conditions prevail on 20 March 2008 ($\phi_{\text{advective}}$ term $\sim 0.83 \times 10^{-4}$ W m^{-3}), as shown in Fig. 11b. Under a negative sign, the SW branch of BSW is weak or completely absent, and the flow at the south of Lemnos Island is narrowed to the
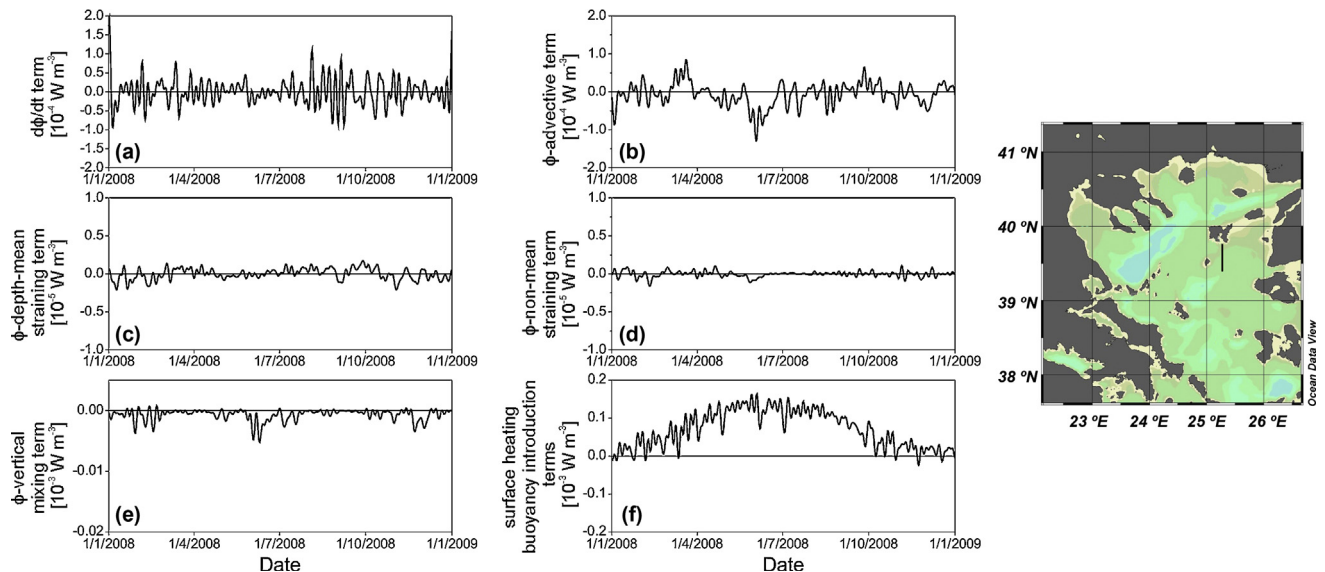
Figure 10 Temporal variability of (a) the $d\phi/dt$-term ($\times 10^{-4}$ W m^{-3}), (b) the ϕ-advective term ($\times 10^{-4}$ W m^{-3}), (c) the ϕ-depth-mean straining term ($\times 10^{-5}$ W m^{-3}), (d) the ϕ-non-mean straining term ($\times 10^{-5}$ W m^{-3}), (e) the ϕ-vertical mixing term ($\times 10^{-3}$ W m^{-3}) and (f) the surface heating buoyancy introduction terms ($\times 10^{-3}$ W m^{-3}), crossing the south-west BSW branch. All terms were smoothed using a low-pass-filter of 0.2 Hz cutoff frequency.
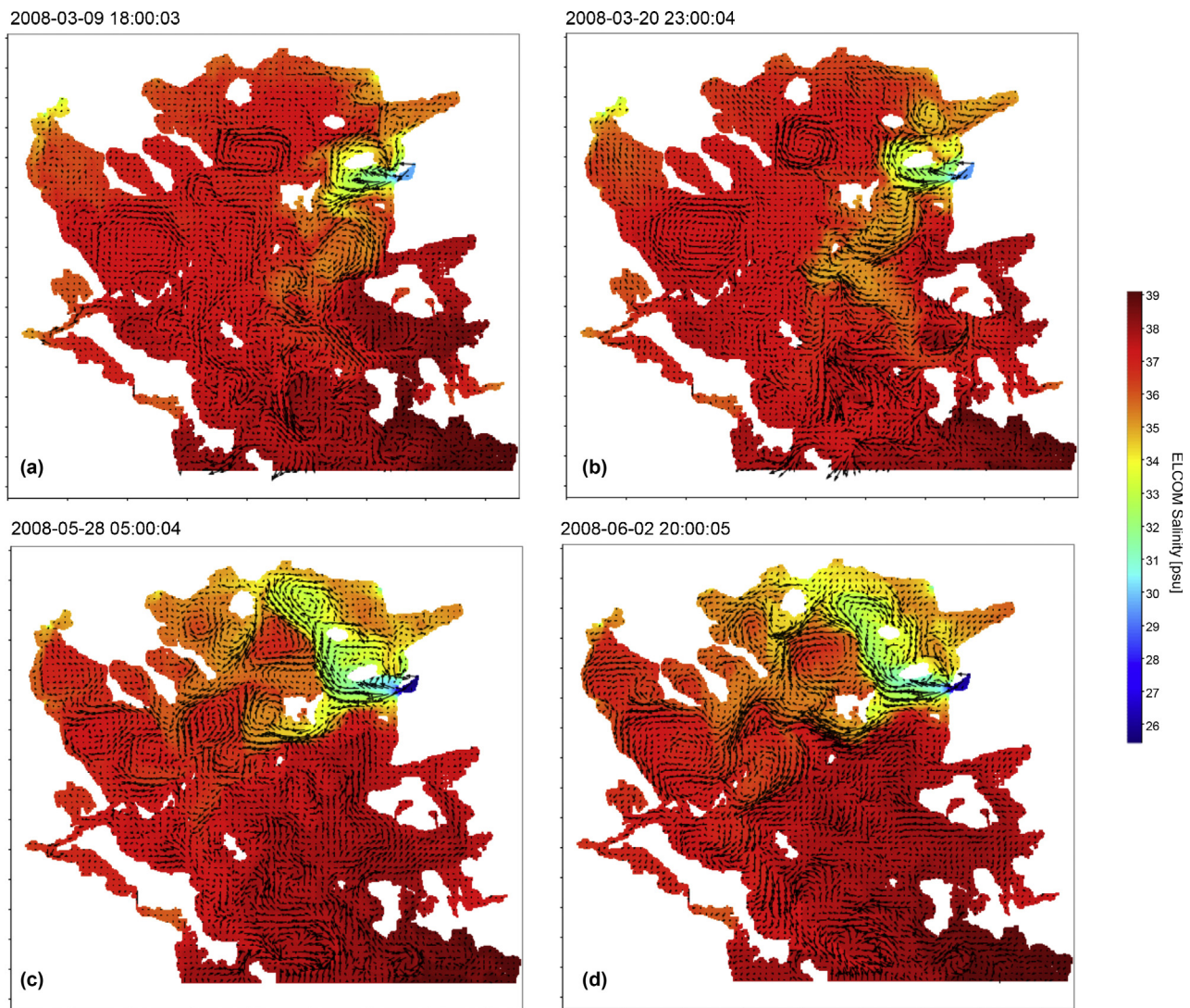
Figure 11 Surface water circulation in North Aegean Sea (a) on 09 March 2008, when the $\phi_{advective}$ term of SW-branch $\sim 0.60 \times 10^{-4}$ W m^{-3}, related to an anticyclone in Sporades Basin, (b) on 20 March 2008, when the $\phi_{advective}$ term of SW-branch $\sim 0.83 \times 10^{-4}$ W m^{-3}, related to an anticyclone in the Sporades Basin, (c) on 28 May 2008, when the $\phi_{advective}$ term of SW-branch $\sim -0.80 \times 10^{-4}$ W m^{-3}, related to a cyclonic flow in the Sporades Basin, and (d) on 2 June 2008, when the $\phi_{advective}$ term of SW-branch $\sim -1.30 \times 10^{-4}$ W m^{-3}, related to a cyclonic flow in the Sporades Basin.

coastal zone, with a westward direction. Strong negative $\phi_{advective}$ term values appear linked to the occurrence of a cyclonic flow in NE Sporades Basin, as on 28 May 2008 ($\phi_{advective} \sim -0.80 \times 10^{-4}$ W m^{-3}; Fig. 11c) and 02 June 2008 ($\phi_{advective} \sim -1.30 \times 10^{-4}$ W m^{-3}; Fig. 11d). Sudden changes in the ϕ-advective term sign occur mostly during August and September (Fig. 10b), leading to consequent changes on the vorticity sign of Sporades Basin flow.

4. Discussion

In this paper, ELCOM model rather successfully simulated the variability of surface circulation and water masses distribution in the North Aegean Sea, producing the rapidly changing surface meso-scale patterns and the water column dynamics under the BSW, meteorological and heat exchange influence.

As seen from model results, the BSW bifurcation at the north and south of Lemnos Island and the relative strength of flow between these branches, determines the variability of the above described meso-scale patterns and the water column stratification-mixing processes, expressed by the potential energy anomaly of the studied system. The north-western BSW flow affects mostly the circulation in the Thracian Sea, feeding sub-basin scale gyres and flows along the Thracian coastline (the Coastal Current) and between Lemnos Basin and Chalkidiki Peninsula (the Rim Current). The strong south-western BSW flow enhances the horizontal density gradients across the BSW-LIW frontal zone and affects the Skiros and Sporades Basins inducing cyclonic–anti-cyclonic flows (the Sporades Eddy). The above described results appear in agreement to the circulation patterns described explicitly by Tzali et al. (2010), Androulidakis and Kourafalou (2011) and Androulidakis et al. (2012).

The potential energy anomaly variability illustrated the importance of BSW outflux in the stratification conditions of the water column. Our results suggest that during the winter the impact of BSW-induced buoyancy on water column stratification is higher by almost two orders of magnitude than that of solar radiation. During spring and summer, solar heat flux gradually increases, allowing BSW buoyancy impact as the dominant ϕ-change term, determining the water column stratification in the Thracian Sea, but only being an order of magnitude higher than the solar radiation effect. At the area of Sporades, solar radiation and buoyancy effects appear comparable during the summer period, while at Chios Basin ϕ-temporal variability shows limited mean-monthly fluctuation and solar radiation dominates the water column dynamics.

To comprehend the impact of BSW pulses advection on the North Aegean Sea, the general dynamic ϕ-equation, as derived by Burchard and Hofmeister (2008), was solved along a meridional transect in the Thracian Sea, utilizing the ELCOM model results for the upper 130 m. The ϕ-advective term crossing the NW branch appears mostly positive, implying the westward transport of the buoyant jet. The term fluctuates strongly in time and receives its highest values during spring and summer, related to the occurrence of a meso-scale eddy spread between Samothraki and Thassos Islands. Based on the modeled flow field, the relative vorticity of this system, known as Samothraki Anticyclone, was calculated, as:

$$\zeta = \frac{\partial v}{\partial x} - \frac{\partial u}{\partial y} \tag{12}$$

and then associated to the ϕ-advective term. Relative vorticity in the Thracian Sea exhibits negative values (mean $\zeta = -1.1 \times 10^{-5}\,\mathrm{s}^{-1}$), indicating the anticyclonic nature of the circulation. A fifth-order polynomial regression between relative vorticity and cross-transect ϕ-advection is shown (Fig. 12), indicating that Samothraki Anticyclone was fed by the north-western branch of the BSW plume. A similar analysis was also performed by Soosaar et al. (2014) on the anticyclonic eddy of the southern Gulf of Riga and its relationship to the wind and horizontal density gradients. Results depicted that this anticyclone was mostly fed by the buoyancy field, being enhanced or reversed by the dominant
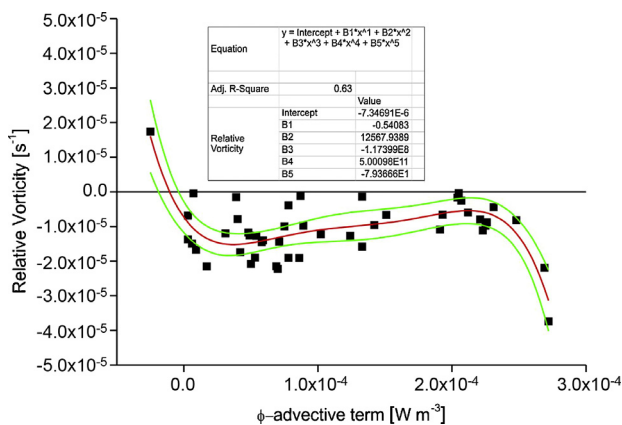
Figure 12 Non-linear regression between the ϕ-advective term crossing the north-west BSW branch and the relative vorticity of Samothraki Anticyclone.

winds. Sylaios (2011) explained that under northerly winds, the anticyclone was pushed towards the north-west of Lemnos Island, while under the influence of south to south-westerly winds, it moved to the north-west of Samothraki Island. As shown by the temporal variation of the ϕ-vertical mixing term (Fig. 9e), in the North Aegean Sea, strong winds ($>15\,\mathrm{m\,s}^{-1}$) tend to destroy the anticyclonic pattern, promoting vertical water column mixing. Indeed, the negative peaks in the temporal variability of term-E (20 February 08; 21 April 08; 30 May 08; 18 June 08; 11 July 08; 20 July 08; 14 September 08) correspond to short-to-medium scale storms with wind speeds between 15 and 20 m s^{-1}.

Based on model results for the Thracian Sea, the baroclinic Rossby radius of deformation for Samothraki Anticyclone was computed, as:

$$R_1 = \frac{c_1}{|f|}, \tag{13}$$

where c_1 is the gravity baroclinic wave speed, estimated by:

$$c_1 = \frac{1}{\pi} \int_{-H}^{0} N(z)\,dz, \tag{14}$$

with $N(z)$ the Brunt-Väisälä frequency. The produced R_1 values during the occurrence of increased positive values in the cross-transect ϕ-advective term exhibits a mean value of 7.5 ± 0.3 km throughout 2008. This result is in agreement with the findings of Androulidakis and Kourafalou (2011), during their numerical experimental tests.

5. Conclusions

In this paper the three-dimensional model ELCOM was adapted, implemented and validated, aiming to derive the hydrodynamic field in the North Aegean Sea. The Black Sea Water outflow and spreading governs surface hydrodynamics, with two distinct branches (NW and SW) at Lemnos Island. Intensive post-processing on the validated model results was carried out, aiming to link BSW buoyancy transfer to NAS water column dynamics and surface meso-scale patterns.

The potential energy anomaly illustrated a significant spatial variability in NAS, due to the variable impact of BSW throughout the system's surface. PEA forcing analysis indicated that BSW induces buoyancy comparable to the solar heating impact on the winter water column stratification of the Thracian Sea. However, in spring and summer, the BSW influence in the Thracian Sea appears up to three times higher than the corresponding solar heating effect. In Sporades, solar radiation and buoyancy impact seem of equal importance for summer water column stratification. Analysis and quantification of the individual PEA terms exhibits the impact of BSW-induced buoyancy on the surface meso-scale patterns of NAS. Indeed, the ϕ-advective term crossing the NW branch exhibits strong relation to the occurrence of Samothraki Anticyclone. A non-linear regression between eddy's relative vorticity and the NW ϕ-advective term was developed, explaining the impact of BSW NW branch on Samothraki Anticyclone.

Similarly, a SW branch enhancement, indicated by the highly positive ϕ-advective values, appears related to the intensification of Sporades Anticyclone. On the contrary,

negative values in the ϕ-advective term appear related to the occurrence of a cyclone in Sporades Basin. This vorticity sign change occurred mostly during August and September 2008, associated to the sudden changes in the ϕ-advection term crossing the SW BSW branch. As shown by the variability of the ϕ−vertical mixing term, strong winds (>15 m s^{-1}) tend to destroy the above meso-scale eddy systems, thus promoting vertical water column mixing in NAS.

References

Alosairi, Y., Imberger, J., Falconer, R.A., 2011. Mixing and flushing in the Persian Gulf (Arabian Gulf). J. Geophys. Res. 116, C03029, 1−14, http://dx.doi.org/10.1029/2010JC006769.

Androulidakis, Y.S., Kourafalou, V.H., 2011. Evolution of a buoyant outflow in the presence of complex topography: the Dardanelles plume (North Aegean Sea). J. Geophys. Res. 116, C04019, http://dx.doi.org/10.1029/2010JC006316.

Androulidakis, Y.S., Krestenitis, Y.N., Kourafalou, V.H., 2012. Connectivity of North Aegean circulation to the Black Sea water budget. Cont. Shelf Res. 48, 8−26, http://dx.doi.org/10.1016/j.csr.2012.08.019.

Barry, M.E., Houdré, F.M., McAlister, A.B., Botelho, D.A., 2009. Three dimensional hydraulic and water quality modelling of the Red Sea: challenges and learnings. In: Proceedings of the 18th World IMACS Congress and MODSIM09 International Congress on Modelling and Simulation, "Interfacing Modelling and Simulation with Mathematical and Computational Sciences", 4142−4148.

Burchard, H., Hofmeister, R., 2008. A dynamic equation for the potential energy anomaly for analysing mixing and stratification in estuaries and coastal seas. Estuar. Coast. Shelf Sci. 77 (4), 679−687, http://dx.doi.org/10.1016/j.csr.2012.08.01910.1016/j.ecss.2007.10.025.

Casulli, V., Cheng, R.T., 1992. Semi-implicit finite difference methods for three dimensional shallow water flow. Int. J. Numer. Meth. Fluids 15, 629−648.

Cordero, S.G., 1999. The use of thermal satellite data in dense water formation studies in the Mediterranean Sea. J. Marine Syst. 20 (1−4), 175−186, http://dx.doi.org/10.1016/S0924-7963(98)00081-5.

Eronat, C., Sayin, E., 2014. Temporal evolution of the water characteristics in the bays along the eastern coast of the Aegean Sea: Saros, Iʐmir, and Gökova bays. Turkish J. Earth Sci. 23, 53−66, http://dx.doi.org/10.3906/yer-1307-4.

Gill, A.E., 1982. Atmosphere−Ocean Dynamics. Int. Geophys. Ser., vol. 30. Academic Press, London, 662 pp.

Hodges, B.R., 2000. Numerical Techniques in CWR-ELCOM (Code Release v.1). CWR Manuscript WP1422 BH. Cent. Water Res., Univ. Western Australia, Perth, 37 pp.

Hodges, B., Dallimore, C., 2001. Estuary and Lake Computer Model: ELCOM Science Manual Code Version 2.0.0. Cent. Water Res., Univ. Western Australia, Perth.

Hoitink, A.J.F., van Maren, D.S., Hoekstra, P., 2011. Mixing and stratification in a tropical tidal embayment subject to a distributed freshwater source. J. Marine Syst. 88 (1), 34−44, http://dx.doi.org/10.1016/j.jmarsys.2011.02.015.

Imberger, J., Patterson, J.C., 1990. Physical limnology. In: Wu, T. (Ed.), Advances in Applied Mechanics, vol. 27, 302−475.

Jedrasik, J., 2005. Validation of the hydrodynamic part of the echohydrodynamic model for the southern Baltic. Oceanologia 47 (4), 543−566.

Kamidis, N., Sylaios, G., Tsihrintzis, V.A., 2011. Modelling Nestos River plume dynamics using ELCOM. Desalin. Water Treat. 33 (1−3), 22−35, http://dx.doi.org/10.5004/dwt.2011.2627.

Karnaska, Y., Maderich, V., 2008. Modelling of seasonal exchange flows through the Dardanelles Strait. Estuar. Coast. Shelf Sci. 79 (3), 449−458, http://dx.doi.org/10.1016/j.ecss.2008.04.019.

Kontoyiannis, H., Kourafalou, V.H., Papadopoulos, V., 2003. Seasonal characteristics of the hydrology and circulation in the Northwest Aegean Sea (eastern Mediterranean): observations and modeling. J. Geophys. Res. 108 (C9), 3302, http://dx.doi.org/10.1029/2001JC001132.

Kopasakis, K.I., Georgoulas, A.N., Angelidis, P.B., Kostovinos, N.E., 2012. Numerical modeling of the long-term transport, dispersion, and accumulation of Black Sea pollutants into the North Aegean coastal waters. Estuar. Coast. 35 (6), 1530−1550, http://dx.doi.org/10.1007/s12237-012-9540-9.

Korres, G., Lascaratos, A., Hatziapostolou, E., Katsafados, P., 2002. Towards an ocean forecasting system for the Aegean Sea. J. Atmos. Ocean Sci. 8 (2−3), 173−200.

Kourafalou, V.H., Barbopoulos, K., 2003. High resolution simulations on the North Aegean Sea seasonal circulation. Ann. Geophys. 21 (1), 251−265, http://dx.doi.org/10.5194/angeo-21-251-2003.

Kourafalou, V., Tsiaras, K., 2007. A nested circulation model for the North Aegean Sea. Ocean Sci. 3 (1), 1−16, http://dx.doi.org/10.5194/os-3-1-2007.

Laval, B., Imberger, J., Hodges, B.R., Stocker, R., 2003. Modeling circulation in lakes: spatial and temporal variations. Limnol. Oceanogr. 48 (3), 983−994, http://dx.doi.org/10.4319/lo.2003.48.3.0983.

Lund-Hansen, L.C., Skyum, P., Christiansen, C., 1996. Modes of stratification in a semi-enclosed bay at the North Sea−Baltic Sea transition. Estuar. Coast. Shelf Sci. 42 (1), 45−54, http://dx.doi.org/10.1006/ecss.1996.0004.

Martin, M., Dash, P., Ignatov, A., Banzon, V., Beggs, H., Brasnett, B., Cayula, J.-F., Cummings, J., Donlon, C., Gentemann, C., Grumbine, R., Ishizaki, S., Maturi, E., Reynolds, R.W., Roberts-Jones, J., 2012. Group for High Resolution Sea Surface temperature (GHRSST) analysis fields inter-comparisons. Part 1: A GHRSST multi-product ensemble (GMPE). Deep-Sea Res. Pt. II 77−80, 21−30, http://dx.doi.org/10.1016/j.dsr2.2012.04.013.

Olson, D.B., Kourafalou, V.H., Johns, W.E., Samuels, G., Veneziani, M., 2007. Aegean surface circulation from a satellite-tracked drifter array. J. Phys. Oceanogr. 37 (7), 1898−1917, http://dx.doi.org/10.1175/JPO3028.1.

Poulos, S.E., Drakopoulos, P.G., Collins, M.B., 1997. Seasonal variability in sea surface oceanographic conditions in the Aegean Sea (Eastern Mediterranean): an overview. J. Marine Syst. 13 (1−4), 225−244, http://dx.doi.org/10.1016/S0924-7963(96)00113-3.

Sayin, E., Eronat, C., Uçkaç, Ş., Beşiktepe, Ş.T., 2011. Hydrography of the eastern part of the Aegean Sea during the East Mediterranean Transient (EMT). J. Marine Syst. 88 (4), 502−515, http://dx.doi.org/10.1016/j.jmarsys.2011.06.005.

Simpson, J.H., 1981. The shelf sea fronts: implications of their existence and behavior. Philos. T. R. Soc. A 302, 531−546.

Simpson, J.H., Sharples, J., Rippeth, T.P., 1991. A prescriptive model of stratification induced by freshwater runoff. Estuar. Coast. Shelf Sci. 33, 23−35, http://dx.doi.org/10.1016/0272-7714(91)90068-M.

Skoulikidis, N.T., Bertahas, I., Koussouris, T., 1998. The environmental state of freshwater resources in Greece (rivers and lakes). Environ. Geol. 36 (1−2), 1−17.

Soosaar, E., Maljutenko, I., Raudsepp, U., Elken, J., 2014. An investigation of anticyclonic circulation in the southern Gulf of Riga during the spring period. Cont. Shelf Res. 78, 75−84, http://dx.doi.org/10.1016/j.csr.2014.02.009.

Spillman, C.M., Imberger, J., Hamilton, D.P., Hipsey, M.R., Romero, J.R., 2007. Modelling the effects of Po River discharge, internal nutrient cycling and hydrodynamics on biogeochemistry of the Northern Adriatic Sea. J. Marine Syst. 68 (1−2), 167−200, http://dx.doi.org/10.1016/j.jmarsys.2006.11.006.

Sylaios, G., 2011. Meteorological influence on the surface hydrographic patterns of the North Aegean Sea. Oceanologia 53 (1), 1−24, http://dx.doi.org/10.5697/oc.53-1.057.

Sylaios, G., Kamidis, N., Anastasiou, S., Tsihrintzis, V.A., 2013. Hydrodynamic response of Thassos Passage (N. Aegean Sea) to Nestos River discharge and meteorological forcing. Cont. Shelf Res. 59, 37—51, http://dx.doi.org/10.1016/j.csr.2013.04.003.

Theocharis, A., Georgopoulos, D., 1993. Dense water formation over the Samothraki and Limnos Plateaux in the north Aegean Sea (Eastern Mediterranean Sea). Cont. Shelf Res. 13 (8—9), 919—939, http://dx.doi.org/10.1016/0278-4343(93)90017-R.

Tuğrul, S., Beşiktepe, S.T., Salihoglu, I., 2002. Nutrient exchange fluxes between the Aegean and Black Seas through the Marmara Sea. Mediterr. Mar. Sci. 3 (1), 33—42, http://dx.doi.org/10.12681/mms.256.

Türkoğlu, M., 2010. Temporal variations of surface phytoplankton, nutrients and chlorophyll *a* in the Dardanelles (Turkish Straits System): a coastal station sample in weekly time intervals. Turkish J. Biol. 34 (3), 319—333, http://dx.doi.org/10.3906/biy-0810-17.

Tzali, M., Sofianos, S., Mantziafou, A., Skliris, N., 2010. Modelling the impact of Black Sea water inflow on the North Aegean Sea hydrodynamics. Ocean Dynam. 60 (3), 585—596, http://dx.doi.org/10.1007/s10236-010-0277-3.

Ünlüata, Ü., Oguz, T., Latif, M.A., Özsoy, E., 1990. On the physical oceanography of Turkish Straits. In: Pratt, L.J. (Ed.), The Physical Oceanography of Sea Straits. Kluwer Acad. Publ., Dordrecht, 25—60.

Vlasenko, V.I., Stashchuk, N.N., Ivanov, V.A., Nikolaenko, E.G., Uslu, O., Benli, H., 1996. Influence of the water exchange through Dardanelles on the thermohaline structure of the Aegean Sea. Bull. Inst. Oceanogr. Monaco, Spec. No. 17, 147—165.

Wiles, P., van Duren, L., Hase, C., Larsen, J., Simpson, J., 2006. Stratification and mixing in the Limfjorden in relation to mussel culture. J. Marine Syst. 60 (1—2), 129—143, http://dx.doi.org/10.1016/j.jmarsys.2005.09.009.

Zervakis, V., Georgopoulos, D., 2002. Hydrology and circulation in the North Aegean (eastern Mediterranean) throughout 1997 and 1998. Mediterr. Mar. Sci. 3 (1), 7—21.

Zervakis, V., Georgopoulos, D., Drakopoulos, P.G., 2000. The role of the North Aegean in triggering the recent Eastern Mediterranean climatic changes. J. Geophys. Res. 105 (C11), 26103—26116, http://dx.doi.org/10.1029/2000JC900131.

Zodiatis, G., Alexandri, S., Pavlakis, P., Jonsson, L., Kallos, G., Demetropoulos, A., Georgiou, G., Theodorou, A., Balopoulos, E., 1996. Tentative study of flow patterns in the North Aegean Sea using NOAA-AVHRR images and 2D model simulation. Ann. Geophys. 14 (11), 1221—1231, http://dx.doi.org/10.1007/s00585-996-1221-1.